High-Performance Hemofiltration via Molecular Sieving and Ultra-Low Friction in Carbon Nanotube Capillary Membranes

Peifu Cheng, Nicholas Ferrell, Carl M. Öberg, Steven F. Buchsbaum, Melinda L. Jue, Sei Jin Park, Dan Wang, Shuvo Roy, Francesco Fornasiero,* William H. Fissell,* and Piran R. Kidambi*

Conventional dialyzer membranes typically comprise of unevenly distributed polydisperse, tortuous, rough pores, embedded in relatively thick ≈20–50 µm polymer layers wherein separation occurs via size exclusion as well as differences in diffusivity of the permeating species. However, transport in such polymeric pores is increasingly hindered as the molecule size approaches the pore dimension, resulting in significant retention of undesirable middle molecules (≥15–60 kDa) and uremic toxins. Enhanced removal of middle molecules is usually accompanied by high albumin loss (≈66 kDa) causing hypoalbuminemia. Here, the scalable bottom-up fabrication of wafer-scale carbon nanotube (CNT) membranes with highly aligned, low-friction, straight-channels/capillaries and narrow pore-diameter distributions (≈0.5–4.5 nm) is demonstrated, to overcome persistent challenges in hemofiltration/hemodialysis. Using fluorescein isothiocyanate (FITC)-Ficoll 70 and albumin in phosphate buffered saline (PBS) as well as in bovine blood plasma, it is shown that CNT membranes can allow for significantly higher hydraulic permeability (more than an order of magnitude when normalized to pore area) than commercial high-flux hemofiltration/hemodialysis membranes (HF 400), as well as greatly enhance removal of middle molecules while maintaining comparable albumin retention. These findings are rationalized via an N-pore transport model that highlights the critical role of molecular flexing and deformation during size-selective transport within nanoscale confinements of the CNTs. The unique transport characteristics of CNTs coupled with size-exclusion and wafer-scale fabrication offer transformative advances for hemofiltration, and the obtained insight into molecular transport can aid advancements in several other bio-systems/applications beyond hemofiltration/hemodialysis.

1. Introduction

Kidney disease is a serious global health problem.[1,2] Chronic kidney disease affects ≈697.5 million people (≈9.1% of the global population) and causes ≈2.6 million deaths annually,[1,2] while acute kidney injury causes ≈1.7 million deaths/year.[3] Causes include high blood pressure, diabetes, auto-immune diseases, drugs, and infections which can severely impair kidney functions necessitating renal replacement therapies such as hemofiltration/hemodialysis, peritoneal dialysis, or kidney transplantation.[1,3] Hemofiltration (convective therapy) and hemodialysis (diffusive therapy) represent extracorporeal processes that aid the removal of unwanted toxins and waste products from blood via selective transport through dialyzer membranes.[4]

Conventional dialyzer membranes are typically formed via phase separation processes and comprise of non-uniformly distributed, polydisperse, tortuous, rough pores embedded in relatively thick ≈20–50 mm polymer layers, for example, cellulose acetate,[5,6] cellulose triacetate,[5,7,8] polysulfone,[4,7–9] polyethersulfone,[4,7,8] polyarylethersulfone,[7,8] polyphenylene,[8] polyarylethersulfone/polyvinylpyrrolidone,[10–13] polymethylmethacrylate,[4,9,13] ethylene

P. Cheng, P. R. Kidambi
Department of Chemical and Biomolecular Engineering
Vanderbilt University
Nashville, TN 37212, USA
E-mail: piran.kidambi@vanderbilt.edu

N. Ferrell, D. Wang
Division of Nephrology
Department of Internal Medicine
The Ohio State University Wexner Medical Center
Columbus, OH 43210, USA

C. M. Öberg
Division of Nephrology
Department of Clinical Sciences Lund
Lund University
Barngatan 2, 21185 Lund, Sweden

vinyl alcohol,[14] and polyacrylonitrile[4,9,15] among others. The pressure-driven flow of blood through polymeric dialyzer membranes yields size-selective transport of smaller waste molecules from blood to dialysate but is also accompanied by saturable adsorption to the polymer, protein caking on the membrane, hindered convection, and hindered diffusion (particularly as the pore size approaches the permeating molecule size). In addition to the cellular elements of blood, plasma contains proteins, for example, clotting factors, hormone-binding proteins, cytokines, antibodies, albumin, etc. that circulate at tightly regulated concentrations and their depletion can jeopardize patient health.[4,13] On the other hand, renal excretion of some proteins, peptides, and other middle molecules (e.g., β_2-microglobulin ≈ 11.8 kDa) is essential for patient health and preventing pathologic accumulation is crucial to avert clinical syndromes such as brown tumors of bone and amyloidosis.[16,17]

The trade-off between selectivity and permeability[18–20] intrinsic to polymeric dialyzer membranes severely limits hemofiltration/hemodialysis, with profound clinical consequences. Notably, the large pore sizes in the tail of the wide log-normal pore-size distributions of conventional polymeric dialyzer membranes can lead to high leakage of desirable plasma proteins, and hindered transport in rough polymeric pores can result in significant retention of undesirable middle-size molecules.[4] For example, conventional high-flux (HF) dialyzer membranes show high retention of albumin (≈ 66 kDa)[21,22] but insufficient removal of middle molecules[4,13] in the ≥ 15–60 kDa range including uremic toxins (Table S1, Supporting Information).[21,22] Indeed, excess mortality and morbidity in dialyzed renal failure have been attributed to imperfect removal of middle molecules.[21,22] On the other hand, high cut-off (HCO) dialyzer membranes show improved removal of middle molecules but also cause clinically significant loss of albumin detrimental to patient health.[4,13]

Additionally, increasing the hydraulic permeability of conventional dialyzer membranes is also desirable to minimize

S. F. Buchsbaum, M. L. Jue, S. J. Park, F. Fornasiero
Physical and Life Sciences
Lawrence Livermore National Laboratory
Livermore, CA 94550, USA
E-mail: fornasiero1@llnl.gov

S. Roy
Department of Bioengineering & Therapeutic Sciences
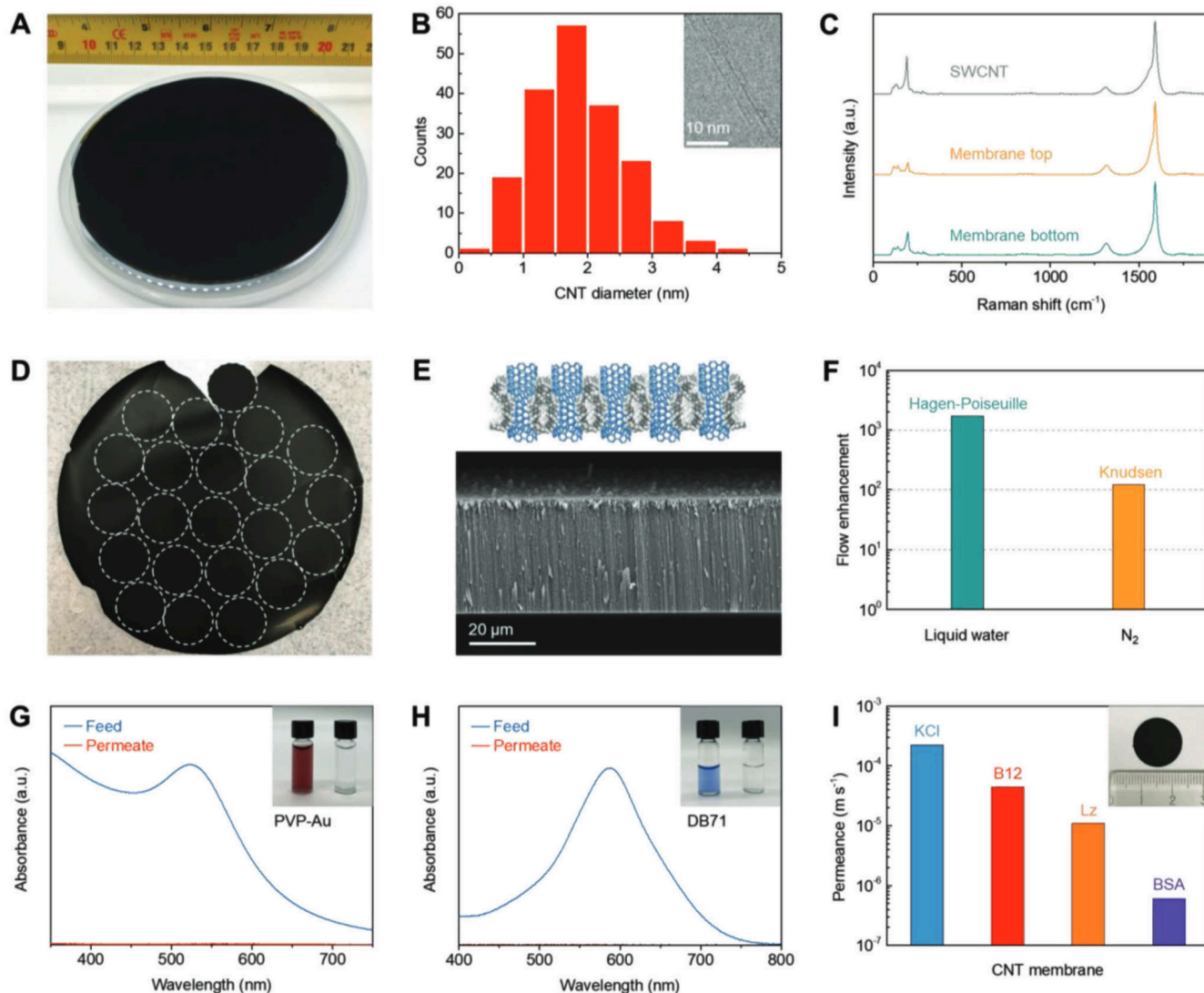University of California
San Francisco, CA 94158, USA

W. H. Fissell
Department of Medicine and Division of Nephrology and Hypertension
Vanderbilt University Medical Center
Nashville, TN 37232, USA
E-mail: william.fissell@vumc.org

W. H. Fissell, P. R. Kidambi
Vanderbilt Institute of Nanoscale Sciences and Engineering
Vanderbilt University
Nashville, TN 37212, USA

P. R. Kidambi
Department of Mechanical Engineering
Vanderbilt University
Nashville, TN 37212, USA

S. F. Buchsbaum
Engineering
Lawrence Livermore National Laboratory
Livermore, CA 94550, USA

the dialyzer size for progress toward portable, wearable, and implantable hemofiltration/hemodialysis devices.[23–27] Hence, enhancing the hydraulic permeability of conventional dialyzer membranes while simultaneously maximizing the removal of middle molecules and uremic toxins, and maintaining albumin losses in the clinically acceptable range for long-term treatment is highly desirable, but remains non-trivial and tremendously challenging.[4]

In this context, near frictionless flow in smooth carbon nanotube (CNT) capillaries/channels with precisely tailored nanopore diameters present potential to transcend inherent limitations of polymeric dialyzers, that is, enable enhanced clearance of middle molecules and uremic toxins while maintaining clinically acceptable albumin loss and very high hydraulic permeability. Indeed, CNT membranes comprising highly ordered, vertically aligned arrays of individual CNT capillaries/channels with narrow pore size distributions have been shown to outperform conventional polymeric membranes with polydisperse tortuous pores in gas/liquid transport,[28,29] nanofiltration,[29–33] ionic/molecular exclusion[30–33] for a range of applications including chemical warfare protection,[31] breathable and protective garments,[29] bacterial resistance,[34] among others. CNT have also been used as additives/fillers in polymeric dialysis membranes (see Table S2, Supporting Information) to enhance the mechanical strength, improve the antifouling property, modify blood compatibility, and tune membrane performance,[35–44] but to the best of our knowledge, the use of CNT channels/capillaries for size-selective mass transport in hemofiltration applications has not been demonstrated.

Here, we demonstrate that vertically aligned CNT capillary membranes with a narrow pore size distribution overcome some of the inherent separation challenges in conventional polymeric hemofiltration/hemodialysis membranes. Using FITC-Ficoll 70 and albumin as probes in PBS solution as well as in bovine blood plasma, we show that CNT membranes with sub-5 nm capillaries allow for an order of magnitude higher hydraulic permeability (when normalized by total pore area) than the commercial high-flux hemofiltration/hemodialysis membranes (HF400), as well as significantly enhanced removal of middle molecules while maintaining comparable albumin retention. We rationalize our findings via an N-pore transport model that indicates molecular conformational flexing and deformations play a significant role during transport within the nanoscale confinement of the CNT channels/capillaries, with profound ramification for the development of next-generation membranes for biological applications.

2. Results and Discussion

We initially describe the CNT membrane fabrication via bottom-up growth using chemical vapor deposition (CVD) followed by post-processing before proceeding to evaluate their performance via diffusive and pressure-driven molecular transport, as well as hemofiltration.

2.1. CNT Growth and Membrane Fabrication

Wafer-scale (4-inch) CNT membranes with sub-5 nm channels/capillaries were fabricated via bottom-up chemical vapor

**ADVANCED
SCIENCE NEWS**

www.advancedsciencenews.com

**ADVANCED
FUNCTIONAL
MATERIALS**

www.afm-journal.de

Figure 1. General structural and transport characterization of the fabricated CNT membranes with sub-5 nm open channels. A) Optical image of wafer-scale vertically aligned CNT forests on Si wafer. B) CNT inner diameter distribution measured from high-resolution TEM images. Inset shows a representative CNT channel. C) Raman spectra of synthesized CNT fibers, top and bottom sides of CNT membrane. D) Optical image of wafer-scale CNT membrane. The circles show the punched regions. E) SEM cross-sectional image of CNT membrane. Inset: schematic of the fabricated membrane in which gaps between vertically aligned open CNT channels are fully filled by polymeric matrix. F) Flow enhancements of liquid water and N_2 gas for CNT membrane. Enhancement factors were calculated by the ratio of the measured permeance (liquid water and N_2) to the theoretical prediction (Hagen–Poiseuille flow and Knudsen flow, respectively). G) UV–vis spectra and optical image of feed and permeate in the filtration through CNT membrane using neutral polyvinylpyrrolidone (PVP)-capped Au nanoparticle solution. H) UV–vis spectra and optical image of feed and permeate in the filtration through CNT membrane using negatively charged Direct Blue 71 dye solution. I) Diffusive permeances of KCl, vitamin B12 (B12), lysozyme (Lz), and bovine serum albumin (BSA) through the CNT membrane. Inset shows the centimeter-scale CNT membrane (punched from the wafer-scale CNT membrane Figure 1D) used for diffusion measurements.

deposition (CVD) growth of vertically aligned CNT forests (**Figure 1**A, see Experimental Section[45,46]), followed by poly-para-xylylene (parylene-N) infiltration into the inter-nanotube spaces within the forest (Figure 1E, top schematic). We note that both parylene-C[32,47–49] and parylene-N[29–32] are biocompatible[50] and can be used as matrix materials to fill the inter-tube gaps of CNTs.[29–32,47–49] Prior studies did not find the parylene matrix type to significantly influence transport behavior.[32] Here, we selected parylene-N for our work because parylene-N is likely to penetrate deeper into high as-

pect ratio features (such as spaces in between CNT channels) due to its lower molecular weight (≈208 Da) than parylene-C (≈277 Da). Subsequently, oxygen plasma was used to remove the excess parylene-N as well as etch the CNT caps and open the CNT capillaries to obtain straight CNT channels/capillaries embedded in a parylene-N film (see Experimental Section),[29–32] forming a nanoporous membrane (Figure 1D). High-resolution transmission electron microscopy (TEM) images show CNT inner diameter distribution from ≈0.5–4.5 nm with an average diameter of ≈1.9 nm (Figure 1B). Raman spectra (Figure 1C)

of the CNTs show characteristic radial breathing modes ≈ 100–$300\,\text{cm}^{-1}$, D $\approx 1315\,\text{cm}^{-1}$, and G $\approx 1590\,\text{cm}^{-1}$ peaks with an I_G/I_D ratio ≈ 6.5–10.3, confirming the formation of single-walled carbon nanotubes (SWCNTs) and the highly graphitic nature of the CNTs.[29,51] Similar Raman spectra (Figure 1C) are found at the top and bottom surface of the CNT membrane indicating the effective removal of any excess parylene-N, which is crucial to allow fluidic transport.[29] Scanning electron microscopy (SEM) cross-sectional image of the CNT membrane ($\approx 34.8\,\mu\text{m}$ thick) shows the gaps between vertically aligned CNT channels appear to be filled with parylene-N (Figure 1E) resulting in CNT capillaries embedded in a parylene matrix (see Figure 1E schematic). Further, we note the mean tensile strength and Young's modulus of the CNT membranes are $\approx 9 \pm 3$ and $\approx 382 \pm 190\,\text{MPa}$, respectively, as reported in prior studies,[29] indicating their suitability for hemofiltration/hemodialysis.

2.2. Pressure-Driven and Diffusive Transport Characteristics of CNT Capillaries/Channels

We first measure liquid water and nitrogen gas flow to benchmark liquid and gas transport in CNT membranes to confirm that fluid transport occurs primarily through the CNT pores (consistent with other prior extensive experimental studies).[29] Pressure-driven water as well as nitrogen gas transport (see Figure 1F and Experimental Section for details) showed 3 and 2 orders of magnitude flow enhancements compared to no-slip Hagen–Poiseuille flow and Knudsen flow, respectively, confirming the frictionless or ultra-low friction nature of fluid flow within the CNT channels/capillaries consistent with prior reports of large slip lengths within CNTs.[29–32] Further, filtration tests of neutral polyvinylpyrrolidone (PVP)-capped Au nanoparticles ($\approx 5\,\text{nm}$ diameter) and negatively charged Direct Blue 71 (DB71) dye molecules (molecular size $3 \times 1.5 \times 1\,\text{nm}$) were used (see Experimental Section) to evaluate transport characteristics of the synthesized CNT membranes. The CNT membranes showed near complete rejection of $\approx 5\,\text{nm}$ PVP-capped Au nanoparticles (Figure 1G) due to steric hindrance, which is fully consistent with the upper bound ($\approx 4.5\,\text{nm}$) of the CNT diameter distribution obtained from TEM imaging (Figure 1B), indicating that the CNTs channels are the primary transport pathways in the synthesized membranes. Complete rejection is also achieved for a smaller dye DB71 dye (Figure 1H) with molecular size $3 \times 1.5 \times 1\,\text{nm}$ within the range of the CNT diameter distribution (Figure 1B). We attribute DB71 rejection (at the very low concentration of $10\,\mu\text{M}$, where ionic strength is very small and Debye length is large)[33] to electrostatic repulsion between the negatively charged dye molecules and the negatively charged carboxylic (COOH) functional groups at the CNT pore entrances introduced by the plasma etching process to open the pores, as detailed in prior studies.[29,30,33]

Diffusion-driven transport through the CNT membranes was measured using four distinct model solutes (Figure 1I) that covered the range of diameter distribution obtained via TEM imaging of CNTs (Figure 1B), that is, KCl (hydrated diameter of K$^+$ ≈ 0.662 and Cl$^-$ $\approx 0.664\,\text{nm}$, $74.55\,\text{Da}$),[18] vitamin B12 (B12, ≈ 1–$1.5\,\text{nm}$, $\approx 1355\,\text{Da}$),[18,52] lysozyme (Lz, ≈ 3.8–$4\,\text{nm}$, $\approx 14.3\,\text{kDa}$),[52] and bovine serum albumin (BSA, average

Stokes diameter $\approx 7\,\text{nm}$, $\approx 66\,\text{kDa}$).[53] Notably, the CNT membrane shows decreasing diffusive permeance with increasing size from KCl ($\approx 2.3 \times 10^{-4}\,\text{m s}^{-1}$) to B12 ($\approx 4.4 \times 10^{-5}\,\text{m s}^{-1}$), Lz ($\approx 1.1 \times 10^{-5}\,\text{m s}^{-1}$), and BSA ($\approx 6 \times 10^{-7}\,\text{m s}^{-1}$), indicating size-selective transport through the CNT membranes. While the average diameter of BSA ($\approx 7\,\text{nm}$) is larger than the maximum size of CNT channels ($\approx 4.5\,\text{nm}$), the short axis ($\approx 4\,\text{nm}$) of BSA (an elongated ellipsoid protein) is smaller, thereby allowing BSA diffusion through CNT membrane.[53] We note that although BSA proteins are also negatively charged, the screening of the electrostatic interaction by the high ionic strength PBS buffer results in diminished charge repulsion,[33] allowing for permeation of BSA through the CNT membrane (Figure 1I) in contrast to DB71 (Figure 1H).

2.3. Filtration Performance of CNT Membranes using Ficoll in PBS

Here, we measured the size-selective sieving performance of the synthesized CNT membranes during filtration using a custom-built pressure-driven cross-flow system (**Figure 2**A, see Experimental Section).[54] The CNT membrane is supported on a Si mask and sandwiched between gaskets, and a neutral filtration probe solution (FITC-Ficoll 70 in PBS, abbreviated as Ficoll) in the feed reservoir is circulated in a continuous perfusion loop with transmembrane pressure serving as the driving force (see Experimental Section). Our rationale for choosing Ficoll as a model probe for the filtration is due to its compact, markedly branched, and cross-linked co-polymer structure of sucrose and epichlorohydrin which is expected to show closer sieving coefficients to proteins[55,56] in comparison to other filtration probes, like dextran (α-1,6-linked d-glucopyranose polymer with flexible linear hydrated random coil structure).[55] The size distribution of Ficoll radii in the feed solution ranged from ≈ 0.8–$12\,\text{nm}$ (Figure 2B). After filtration, the permeate solution shows a clear shift in the Ficoll signal curve towards smaller radii with a significant decrease in permeation for molecules > 6 nm in radii (Figure 2B). Next, filtration was also performed with a customized dialyzer fabricated by assembling some commercial high-flux HF400 hemofiltration/hemodialysis fibers from the cartridge (see Figure S2, Supporting Information and Experimental Section) using the same Ficoll feed under similar transmembrane pressures. The filtration results showed a significant downward shift in the permeation curve, albeit with a similar filtration range (≈ 0.8–$6\,\text{nm}$ molecular radius, Figure 2B).

Sieving coefficients[4] (SC) as a function of Ficoll molecular radius (and/or molecular weight) were computed by dividing the Ficoll concentration in the permeate by that in the feed. The SC of the HF400 membrane reached the maximum value ($\approx 83.3\%$) for molecular radius of $\approx 1.4\,\text{nm}$ (molecular weight of $\approx 5.7\,\text{kDa}$) and subsequently decreased with increasing radius (Figure 2C,D). In contrast, the SC of the CNT membrane reached the maximum value ($\approx 100\%$) for molecular radius of $\approx 2.3\,\text{nm}$ (molecular weight of $\approx 16.5\,\text{kDa}$) and then decreased with increasing radius. To facilitate a quantitative comparison of SC, we use a logarithmic scale of the Y-axis (see Figure S3, Supporting Information) and observe that the molecular radius (or molecular weight) cut-offs corresponding to SC = 10%, 1%, and 0.01% are $\approx 4\,\text{nm}$ (or
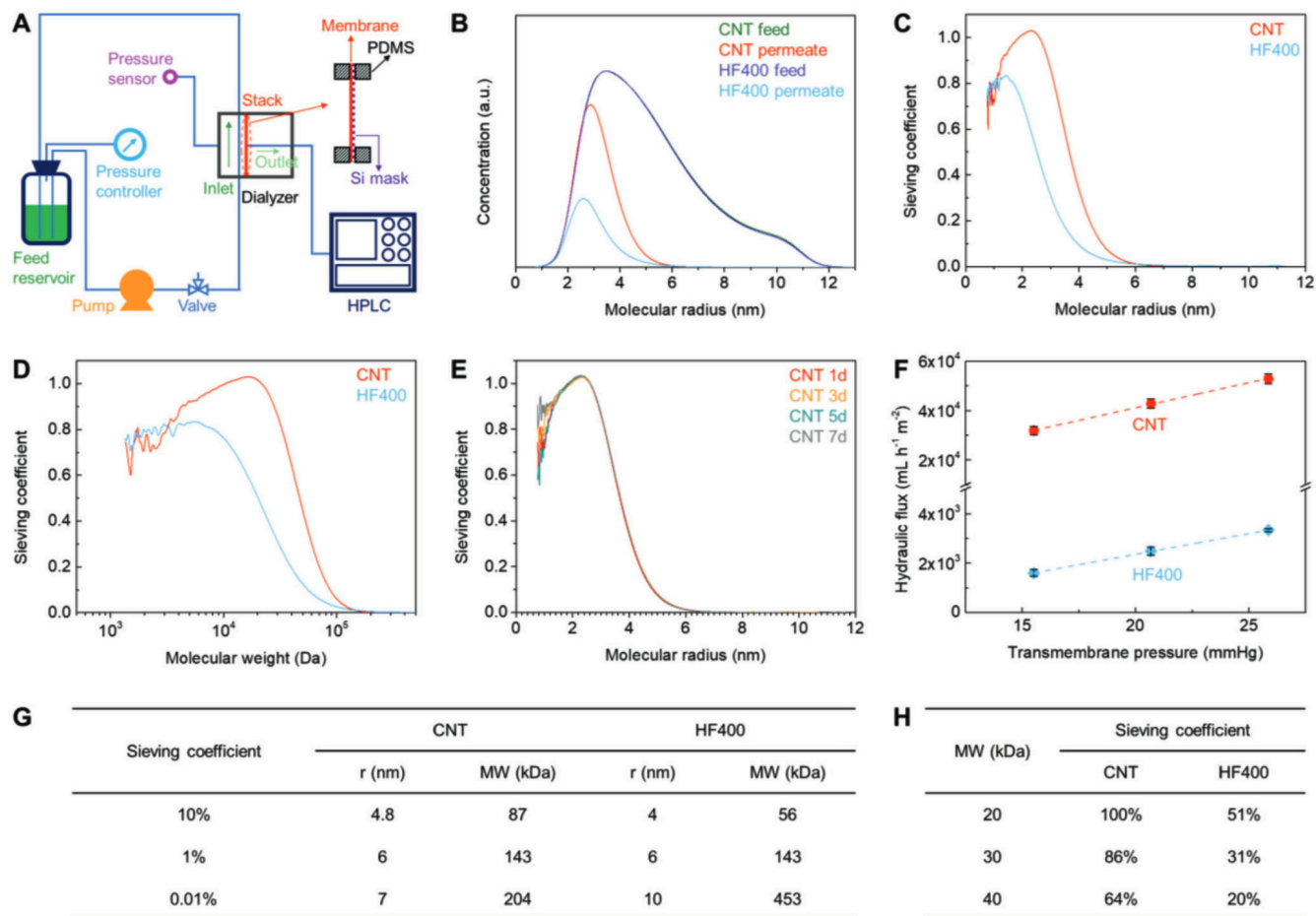
Figure 2. Filtration performance of CNT membrane compared with commercial high-flux HF400 membrane using Ficoll in PBS solution as the probe. A) Schematic diagram of the custom-designed pressure-driven cross-flow filtration system. CNT membrane was backed up by a Si mask and sandwiched between two polydimethylsiloxane (PDMS) gaskets. B) Ficoll concentrations in the feed and permeate solutions from filtration across CNT and HF400 membranes. C) Ficoll sieving coefficient (SC) as a function of molecular radius for CNT and HF400 membranes. D) Ficoll sieving coefficient (SC) as a function of molecular weight for CNT and HF400 membranes. E) Stability test of CNT membrane under constant pressure for 7 days. F) Hydraulic flux of Ficoll solution permeation as a function of applied pressure for CNT and HF400 membranes. Error bars indicate one standard deviation. We note the hydraulic flux is calculated based on the effective membrane areas (accounting for the porosities of CNT and HF400 membranes). Also see Figure S5, Supporting Information for hydraulic permeability for CNT and HF400 without accounting for pore area. G) Molecular radius (r) or molecular weight (MW) cut-offs corresponding to SC = 10%, 1%, and 0.01% for CNT and HF400 membranes. H) Sieving coefficient values of CNT and HF400 membranes at 20, 30, and 40 kDa molecular weight.

$\approx$56 kDa), $\approx$6 nm (or $\approx$143 kDa), and $\approx$10 nm (or $\approx$453 kDa) for HF400 membrane, respectively (Figure 2 and table in Figure 2G). In contrast, the CNT membrane shows that the molecular radius (or molecular weight) cut-offs corresponding to SC = 10%, 1%, and 0.01% are $\approx$4.8 nm (or $\approx$87 kDa), $\approx$6 nm (or $\approx$143 kDa), and $\approx$7 nm (or $\approx$204 kDa), respectively (Figure 2 and table in Figure 2G). In other words, with an increase in Ficoll molecular radius (or molecular weight), the SC of the HF400 membrane decreases gradually, while the SC of the CNT membrane decreases steeply. We further compared the SC values of membranes at 20, 30, and 40 kDa molecular weight, and obtain 51%, 31%, and 20% for HF400 membrane, as well as 100%, 86%, and 64% for CNT membrane, respectively (Figure 2 and table in Figure 2H). Thus, albeit both CNT and HF400 membranes show size-dependent selectivity of Ficoll, the CNT membrane significantly enhances the removal of middle molecules ($\approx$15–60 kDa) compared to the HF400 membrane.

Notably, the hydraulic flux of the Ficoll solution in PBS was also measured as a function of transmembrane pressure (Figure 2F) and normalized by the total pore area for the CNT ($\approx$5% porosity) and HF400 ($\approx$50% porosity) membranes. The hydraulic fluxes of both CNT and HF400 membranes increase linearly with increasing applied pressure (Figure 2F) indicating that liquid transport through CNT membrane is non-compressible[54] as in commercial HF400 membrane. The hydraulic permeability of CNT membrane $\approx$2032.8 mL h^{-1} mmHg^{-1} m^{-2} is an order of magnitude higher than that of the HF400 membrane ($\approx$168.4 mL h^{-1} mmHg^{-1} m^{-2}, Figure 2F). This result is consistent with prior reports of CNT membrane permeances surpassing those of commercial polymeric membranes in the nanofiltration and ultrafiltration regimes.[30] We attribute it to the large slip lengths[28,57] at the CNT inner walls, as revealed by pure-water transport rates three orders of magnitude larger than predictions from no-slip Hagen–Poiseuille law (Figure 1F).
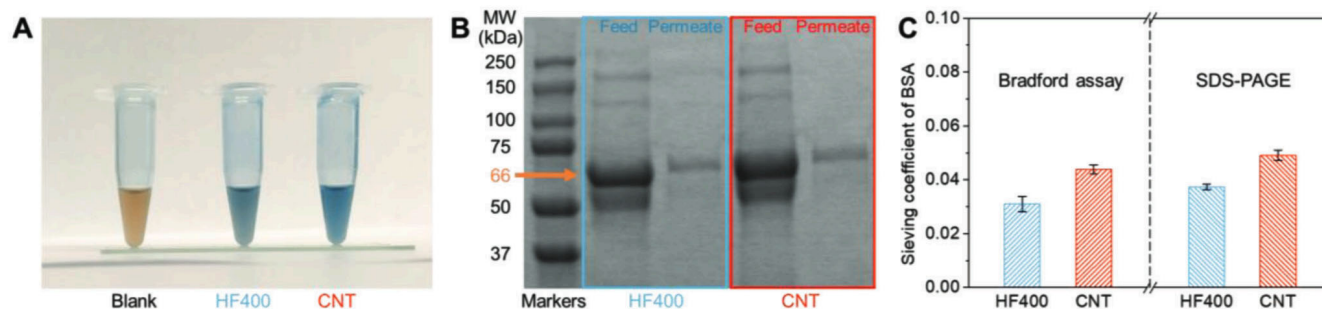
Figure 3. Sieving coefficients of BSA for CNT membrane compared with commercial high-flux HF400 membrane during filtration/hemofiltration. A) Optical image of the blank G-250 dye (left), G-250 dye with the addition of permeate from BSA/PBS feed across the HF400 membrane (middle), and G-250 dye with the addition of permeate from BSA/PBS feed across CNT membrane (right). B) Optical image of Precision Plus Protein markers (left), plasma feed and permeate across the HF400 membrane (middle), and plasma feed and permeate across CNT membrane (right). C) Sieving coefficients of BSA through the HF400 and CNT membranes evaluated by Bradford assay (using BSA in PBS feed) and SDS-PAGE method (using plasma feed), respectively. Error bars indicate one standard deviation.

We also report the measured hydraulic permeability without accounting for the membrane porosity (Figure S5, Supporting Information) and note that the measured hydraulic permeability of the CNT membrane (101.6 mL h^{-1} mmHg^{-1} m^{-2}) is still significantly higher than that of HF400 membrane (84.2 mL h^{-1} mmHg^{-1} m^{-2}), despite porosity of $\approx$5% for CNT membranes compared to $\approx$50% for HF 400. Furthermore, CNT membrane shows a much higher Darcy permeability (1.5 × 10^{-16} m^2) than HF400 membranes (1.2 × 10^{-17} m^2).

To investigate the stability of the CNT membrane, we performed the Ficoll filtration experiments over 7 days. Similar filtration performances were achieved at different time points, indicating the long-term stability of CNT membranes (Figure 2E). The noise in the signal at lower molecular radius < 1.5 nm (molecular weight < 6.3 kDa, Figure 2C,D,E) is attributed to the very low Ficoll concentration in solution at these low molecular weight ranges. We further performed Ficoll filtration measurements using multiple CNT membranes from the same batch (Figure 1D) and obtained very similar results (Figure S4, Supporting Information), indicating the reliability and reproducibility of the CNT membrane fabrication process as well as the resulting transport characteristics.

2.4. Albumin Retention of CNT Membranes

For hemofiltration, in addition to enhanced clearance of middle molecules ($\approx$15–60 kDa), it is also important to control albumin ($\approx$66 kDa) loss within clinically acceptable ranges.[4] We note that although more compact than dextran, Ficoll molecules are more deformable than proteins[56,58] and uncharged, while albumin is negatively charged. Hence, we cannot infer albumin retention directly from the SC curve of Ficoll. Hence, we probed albumin transport by using BSA in PBS solution (40 g L^{-1}, which is close to the concentration of human serum albumin[76] $\approx$35–50 g L^{-1}) using the same filtration system, albeit with a marginally higher transmembrane pressure (0.6 psi, rather than 0.3–0.5 psi, see Experimental Section) to account for the relatively high oncotic pressure ($\approx$0.31 psi)[80] from the BSA solution which counteracts the pressure differential.

The permeate was evaluated with Bradford Protein Assay[59] (see Experimental Section and Figure S6, Supporting Information) since only one type of protein (i.e., BSA) was used in the feed. When the permeate across HF400 or CNT membrane is added, the blank Coomassie dye turns from a brown (**Figure 3**A) to a blue color due to protein binding to dye, indicating BSA permeation through both HF400 and CNT membranes. The SC of BSA across the CNT membrane is $\approx$4.4% (Figure 3C), which is in good agreement with the small BSA leakage seen in the diffusion-driven transport experiments (Figure 1I), whereas the SC of BSA for the HF400 membrane is $\approx$3.1%. Thus, the albumin retention for CNT membranes at $\approx$95.6% is comparable to that of HF400 membranes at $\approx$96.9% in PBS solutions.

To evaluate the albumin retention in simulated body conditions, we also performed hemofiltration runs using platelet-poor plasma derived from bovine blood (see Experimental Section and Figure S8, Supporting Information) and sodium dodecyl sulfate-polyacrylamide gel electrophoresis (SDS-PAGE) was used to measure feed and permeate protein concentrations.[60] Protein bands in the feed and permeate solutions from HF400 and CNT membranes were observed between the 75 and 50 kDa markers (Figure 3B), consistent with the presence of albumin ($\approx$66 kDa). The permeate albumin bands are much lighter and thinner than the feed albumin bands for both HF400 and CNT membranes, demonstrating that the albumin leakages across both membranes are very small (Figure 3B). Quantification of the gels analysis (see Experimental Section and Figure S7, Supporting Information) shows that the SCs of albumin using plasma feed for CNT (4.9%) and HF400 (3.7%) membrane are also similar to each other and to the results using BSA in PBS solution (Figure 3C).

2.5. Hemofiltration Performance of CNT Membranes using Ficoll in Bovine Blood Plasma

We also measured filtration using Ficoll in bovine blood plasma (Figure S9, Supporting Information) to investigate the permselectivity of CNT membrane in simulated body fluids. After hemofiltration, size-exclusion chromatograms of feed and
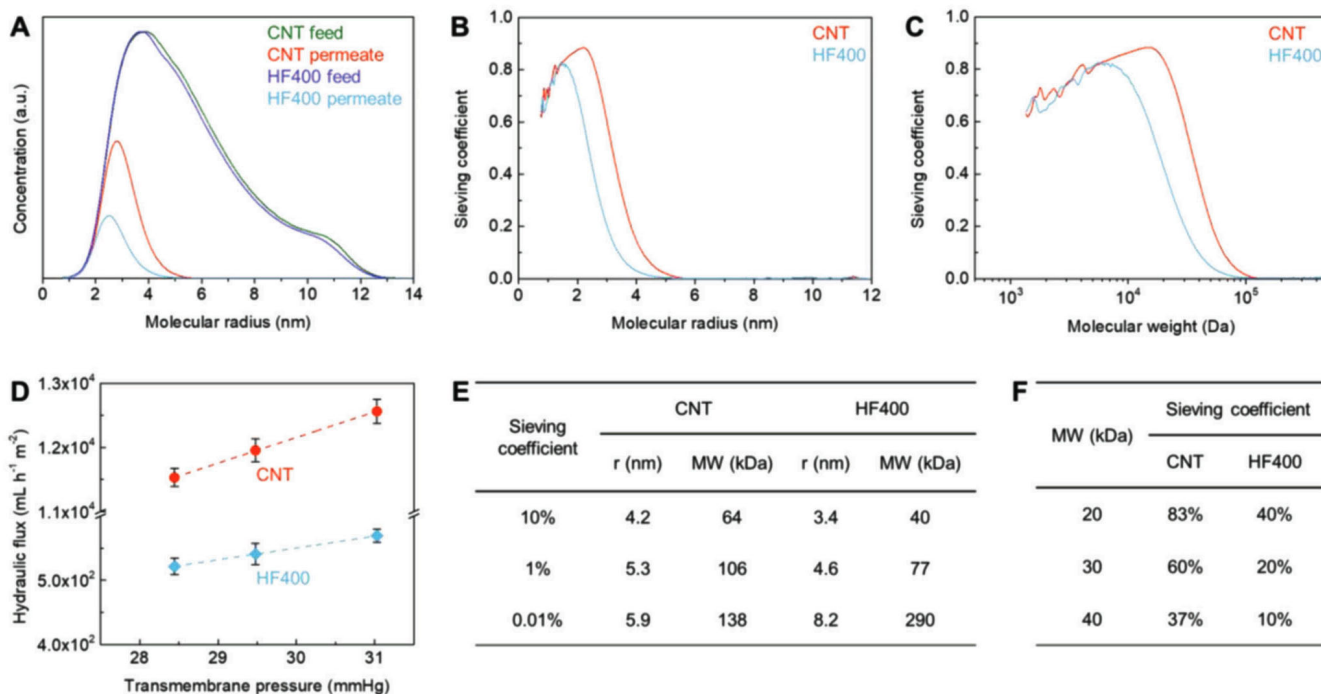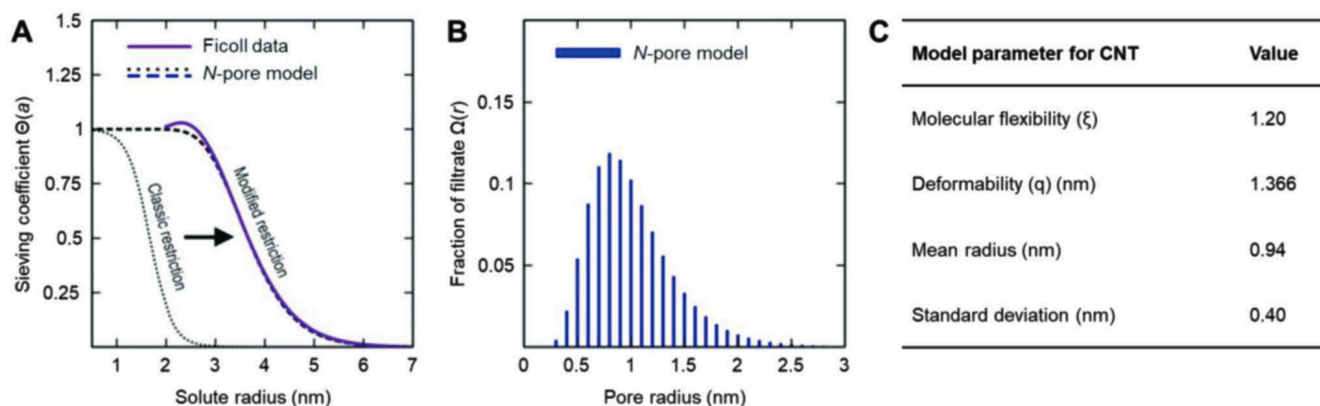
Figure 4. Hemofiltration performance of CNT membrane compared with commercial high-flux HF400 membrane using Ficoll in blood plasma as the probe. A) Ficoll concentrations in the feed and permeate solutions from hemofiltration across CNT and HF400 membranes. B) Ficoll sieving coefficient (SC) as a function of molecular radius for CNT and HF400 membranes. C) Ficoll sieving coefficient (SC) as a function of molecular weight for CNT and HF400 membranes. D) Hydraulic flux of Ficoll solution permeation from Ficoll in blood plasma feed as a function of applied pressure for CNT and HF400 membranes. Error bars indicate one standard deviation. We note the hydraulic flux is calculated based on the effective membrane areas (accounting for the porosities of CNT and HF400 membranes). Also see Figure S11, Supporting Information for hydraulic permeability for CNT and HF400 without accounting for pore area. E) Molecular radius (r) or molecular weight (MW) cut-offs corresponding to SC = 10%, 1%, and 0.01% for CNT and HF400 membranes. F) Sieving coefficient values of CNT and HF400 membranes at 20, 30, and 40 kDa molecular weight.

permeate (CNT or HF400) showed retention of larger molecular weight Ficoll (**Figure** 4A–C). The SC curves (Figure 4B,C) also demonstrate that when using Ficoll in plasma as the feed, the CNT membrane can still significantly enhance the removal of large middle molecules compared with the HF400 membrane. Further comparison of molecular weight retention onset (MWRO) and molecular weight cut-off (MWCO) values between commercial hemodialysis/hemofiltration membranes and our work are shown in Table S1, Supporting Information, and note we used Ficoll, instead of dextran in our work. Notably, our CNT membrane shows MWRO larger than the medium cut-off (MCO) commercial membranes and MWCO between HF and MCO commercial membranes, indicating significantly enhanced sieving performance (Table S1, Supporting Information). We further compare the SC of albumin (Figure 3C) with that of Ficoll at an equivalent molecular weight (≈66 kDa, see Figure S12, Supporting Information). For the HF400 membrane, the SC of Ficoll (1.9%) is lower than that of albumin (3.7%), indicating that polydispersity and torturous rough pores in the HF400 membrane result in similarly hindered transport of Ficoll and albumin molecules. For the CNT membrane, the SC of Ficoll (8.9%) is higher than that of albumin (4.9%) since Ficoll has a range of shapes and is more flexible/deformable than albumin when passing through the straight and smooth CNT channels.

Notably, the apparent molecular weight roll-off in experiments with plasma (Figure 4B,C) appears at a lower molecular weight than in experiments with PBS (Figure 2B–D). With Ficoll in plasma as the feed (compared to Ficoll in PBS in Figure 2G,H), the molecular radius (or weight) cut-offs corresponding to SC = 10%, 1%, and 0.01% decrease from 4.8 nm (or 87 kDa), 6 nm (or 143 kDa), and 7 nm (or 204 kDa) to 4.2 nm (or 64 kDa), 5.3 nm (or 106 kDa), and 5.9 nm (or 138 kDa) for the CNT membrane, respectively (Figure 4E and Figure S10, Supporting Information). In comparison, for HF 400 membrane, the molecular radius (or weight) cut-offs corresponding to SC = 10%, 1%, and 0.01% decrease from 4 nm (or 56 kDa), 6 nm (or 143 kDa), and 10 nm (or 453 kDa) for Ficoll in PBS (Figure 2G,H) to 3.4 nm (or 40 kDa), 4.6 nm (or 77 kDa), and 8.2 nm (or 290 kDa) for Ficoll in plasma (Figure 4E and Figure S10, Supporting Information), respectively. We also compare the SC values of both membranes at 20, 30, and 40 kDa molecular weight, and find the values decrease when using Ficoll in plasma for HF400 membrane (42%, 20%, and 10%), as well as CNT membranes (83%, 60%, and 37%), respectively (Figure 4F), compared to Ficoll in PBS as the feed (Figure 2H). These observations indicate that exposure to bovine blood plasma results in a narrowing of the permeating molecule sizes for both CNT as well as HF 400 membranes, which is consistent with prior literature in the field[11] and typically attributed

**ADVANCED
SCIENCE NEWS**

www.advancedsciencenews.com

**ADVANCED
FUNCTIONAL
MATERIALS**

www.afm-journal.de

Figure 5. N-pore model for predicting the sieving coefficient curve of Ficoll across CNT membrane by altering its deformability (q). A) Predicted sieving coefficient curve of Ficoll across CNT membrane based on B) the measured pore size distribution using C) model parameters (molecular flexibility of 1.2 and deformability of 1.366).

to the deposition of a protein layer on the membrane[11] or crowding at the pore entrance.

Additionally, we also measured the hydraulic permeability for both CNT and HF400 membranes using Ficoll in plasma solution as the feed (Figure 4D and Experimental Section). Both CNT and HF400 membranes are less permeable, owing to the inevitable protein adsorption or crowding at the pore entrance. Despite protein adsorption, the hydraulic permeability (taking into account the effective membrane area) of the CNT membrane still reaches ≈398.3 mL h^{-1} mmHg^{-1} m^{-2}, which is ≈20 times higher than that of the HF400 membrane (≈18.4 mL h^{-1} mmHg^{-1} m^{-2}, Figure 4D). We also report the as-measured hydraulic permeability of hemofiltration without accounting for the vastly different membrane porosities in Figure S11, Supporting Information. Notably, the CNT membrane still showed a significantly higher value ≈19.9 mL h^{-1} mmHg^{-1} m^{-2} compared to HF400 membranes ≈9.2 mL h^{-1} mmHg^{-1} m^{-2}).

2.6. Modeling Molecular Transport in CNT Capillaries/Channels

To understand the transport characteristics of Ficoll through the CNT membranes, we performed simulations using a model with N-parallel pores for predicting the SC curve of Ficoll by varying its deformability (q), defined as the right-shift (in nm) of the sieving curve compared to that of a solid solute sphere.[56,58] An SC curve of Ficoll transport through the CNT membranes is computed based on the measured pore size distribution (Figure 1B) by adjusting the model parameters, that is, molecular flexibility of 1.2 and deformability of 1.36 for Ficoll (**Figure 5**C). This results in agreement with the measured SC (Figures 2C,E and 5A). Changes to the molecular flexibility and deformability explain the shift in the SC from 0–2.5 nm for rigid spheres to 0–6 nm for Ficoll (Figure 5A,C). Taken together, these observations help explain the measured radius cut-off of ≈6 nm for Ficoll in our filtration experiments (Figure 2B,C,E) with a TEM pore diameter distribution of the CNTs ≈0.5–4.5 nm (Figure 1B). These observations can also potentially help explain differences between the sieving coefficient of Ficoll (relatively more deformable, Figure 4) and albumin in plasma (Figure 3) for CNT membrane (Figure S12, Supporting Information). Similar modeling was also

performed for HF400 membranes based on the SC curve of Ficoll (Figure 2C), assuming the molecular flexibility ≈1.2 and no deformability, resulting in a polydisperse distribution of pores (Figure S13A–C, Supporting Information). We hypothesize the model-predicted polydisperse pores in HF 400 membranes results in the experimentally observed less steep SC curve compared to CNT membranes. Hence, we assign the origins of enhanced larger middle molecule clearance to the straight transport pathway as well as the narrow pore size distribution of the CNT membranes. Finally, the N-pore transport model provides a theoretical framework[61–65] to describe the observations from the size-selective transport measurements and highlights the role of molecular conformational flexing and deformation during transport within nanoscale confinements. We also note the mechanism proposed here is fully consistent with prior observations in hemofiltration[61–65] as well as other systems in literature (e.g., n-hexane enters the tight single-wall carbon nanotube pore (≈0.42 nm diameter) at its stretched state (elongating by nearly 11.2%)),[66] that suggests its wider relevance and applicability.

3. Conclusion

In conclusion, we have demonstrated large-area vertically aligned CNT membranes with sub-5 nm channels/capillaries to enable overcoming persistent challenges in hemofiltration/hemodialysis. Compared with commercial HF 400 hemofiltration/hemodialysis membranes, the narrow pore diameter distribution (≈0.5–4.5 nm) and highly ordered low-friction straight channels/capillaries in CNT membranes allow for significantly enhanced removal of middle molecules (≈15–60 kDa), while maintaining comparable albumin (≈66 kDa) retention. The sharper molecular weight cut-off has been rationalized using an N-pore transport model which accounts for conformational flexing and deformation of Ficoll molecules during transport within the nanoscale confinement of the CNT channels/capillaries. Further, CNT membranes offer an order of magnitude higher hydraulic permeability (normalized by pore area) than commercial HF400 membranes. The higher hydraulic permeability, coupled with enhanced sieving performance and wafer-scale bottom-up fabrication presents the potential to aid miniaturization of dialyzer sizes for progress towards wearable, portable, and

ADVANCED
SCIENCE NEWS
www.advancedsciencenews.com

ADVANCED
FUNCTIONAL
MATERIALS
www.afm-journal.de

implantable hemofiltration/hemodialysis devices. The insights from our work coupled with future work on hemocompatibility such as hemolysis tests, clotting time assessment, and platelet adhesion test will inform and guide developments in CNT membranes for hemofiltration. We expect our work to not only offer transformative advances in hemofiltration/hemodialysis but also allow for insights into molecular transport that can help advance membrane design for other biological systems and applications beyond.

4. Experimental Section

Synthesis of Carbon Nanotube Forests: Vertically aligned carbon nanotubes were grown on 100 mm Si (100) wafers that were coated with a $Fe/Mo/Al_2O_3$ catalyst stack by electron-beam evaporation without breaking the vacuum between layers.[30,32,45,46] Nominal thicknesses of the catalyst layers used in this study ($Fe/Mo/Al_2O_3$ = 5.5/0.5/400 Å) were recorded in situ by a quartz crystal monitor during deposition. Synthesis of small diameter SWCNTs at 4-in. wafer scale was performed at low pressure (80 mbar) in a cold-wall furnace (AIXTRON Black Magic Pro, 6 in.), featuring a 6-in. heater stage and gas showerhead. The chamber was pumped down below 0.2 mbar prior to initiating the growth recipe, which started with a thermal annealing step in a reducing environment before introducing the hydrocarbon feedstock growth gas (C_2H_2). The specific recipe used in this study consisted of a) annealing: ramp with top heater at 300 °C min^{-1} to 700 °C and bottom heater at 300 °C min^{-1} to 800 °C at 80 mbar in H_2/Ar = 700/200 sccm and hold for 2 min at 800 °C; b) growth: switch the gas mixture to $C_2H_2/H_2/Ar$ = 4/700/400 sccm at 80 mbar (with 20 sccm Ar through a bubbler containing DI water, resulting in ≈50 ppm of water) and hold for 13 min before evacuating and cooling the chamber in Ar. This low-pressure recipe produced forests with 34.8 ± 0.3 µm thickness and number density of 1.83×10^{12} cm^{-2}.

Fabrication of CNT Membranes: The composite membranes were created by vapor deposition of ≈12 000 Å of poly-para-xylylene (parylene N) within vertically aligned CNT forests as described in detail elsewhere (Specialty Coating Systems, Indianapolis, IN).[29–32] Excess parylene and CNT end caps were removed using an inductive-super-magnetron (ISM) generated oxygen plasma (ULVAC NE-550EXa). The antenna power was set to 200 W, bias power to 25 W, chiller to 0 °C, pressure to 0.5 Pa, and O_2 flow rate to 99 sccm. To estimate the etch rate under these etch conditions, the average thickness of a parylene N layer on a silicon wafer was measured after multiple etch steps using non-contact spectro-reflectometry (TOHO 3100, NanoSpec). The etch time for the 4-in diameter CNT composite used in this study was 460 s. The etched composite wafers were then immersed in 37% hydrochloric acid (Sigma-Aldrich, product # 320331) for 5 to 24 h to dissolve the alumina and catalyst layer between the CNTs and the Si-wafer and delaminate the CNT-parylene composite. The free-standing composites were cut into smaller coupons. For filtration/hemofiltration studies with Ficoll, 1.6 cm diameter free-standing coupons were used without further processing. For gas and water permeance quantification and for selectivity tests, the coupons were first glued to 0.005-inch-thick Kapton–HN frames (Hardman Double/Bubble epoxy, product # 04007). The CNT membranes used for these studies had an average line-to-line diameter of ≈2.21 nm, height of 34.8 ± 0.3 µm, and CNT number density of 1.83×10^{12} cm^{-2} (Figure 1D).

Characterization of CNT Forests and Membranes: High-resolution transmission electron microscopy (HRTEM) was used to quantify the CNT diameter distribution and number of walls per CNT with a sample number N = 190 (image processing performed using custom MATLAB script). A JEOL 2100-F field-emission analytical TEM, operating at 200 kV, ≥ 150 k× magnification, with a pixel resolution of ≤ 0.05 nm was used. Samples were prepared by dispersing CNT forests in ethanol with ultrasonication and subsequently drop-casting the dispersion onto Cu TEM grids coated with Formvar. CNT diameter was defined here as the distance between the CNT wall centers and is equal to 2.21 ± 0.72 nm. The inner pore diameter (≈1.9 nm) was 0.34 nm smaller than the reported average CNT diameter defined above.

Scanning electron microscopy (SEM) was performed with a Zeiss Gemini Ultra-55 analytical field emission SEM or a ThermoFisher Scientific Apreo S high-resolution SEM at 5–10 kV accelerating voltage. The mean number density ρ_n (cm^{-2}) was quantified from the mass increase of the Si substrate after CNT growth[67] and from the forest height with the following equation.

$$\rho_n = \frac{\rho_m}{\pi d / SSA_G} \tag{1}$$

where ρ_m is the CNT volumetric mass density, d is the mean SWCNT diameter measured by TEM, and SSA_G is the specific surface area of graphene, 1315 m^2 g^{-1}. The volumetric mass density was obtained from the mass gain of the catalyst-coated silicon wafer after CNT growth and calculated according to Equation (2).

$$\rho_m = \frac{m_{CNT}}{h_{CNT} A_{CNT}} \tag{2}$$

where m_{CNT} is the mass of the CNT forest, h_{CNT} is the height of the CNT forest, and A_{CNT} is the CNT growth area. Approximately 30 mg of vertically aligned carbon nanotubes (VACNTs) were grown on each wafer and measured with 0.1 mg precision. A possible error in m_{CNT} quantification was due to amorphous carbon content amounts to < 5%, as revealed by previous TGA measurements.[45,46] For this work, the CNT forest height (34.8 µm) was assumed equal to the average membrane thickness measured by SEM at multiple sample locations.

Micro-Raman spectroscopy of the top surface of produced CNT forests and of both surfaces of the CNT-parylene N membranes was performed using a Renishaw InVia Qontor Raman spectrometer with excitation wavelength λ = 633 nm, a grating of 1200 lines per mm, and a 50× long-working-distance objective. The final spectra used for analysis were generated by averaging over ten 1-s collections at 5% power. Each spectrum was baseline subtracted with an 11th-order polynomial prior to data analysis. The mean structural quality of the CNT before and after parylene N deposition was quantified by calculating the ratio between the peak areas of the D-band (≈1315 cm^{-1}) and G-band (≈1590 cm^{-1}). Measured G/D were 10.3 ± 0.5, 6.5 ± 1.0, and 6.7 ± 0.9 for as-grown CNTs, top and bottom surfaces of the CNT-parylene N composite, respectively.

Gas Transport Measurements: N_2 permeance of SWCNT membranes was measured in custom-built dead-end permeation cells at ambient conditions (21 °C), as previously reported.[29] Typically, the mass flow rate was recorded at 8 pressure points up to 4 psi with a downstream mass flow meter. N_2 permeance measurements were used to gauge the degree of membrane pore opening and as a screening tool to qualitatively identify the presence of large defects. Since transport through a few nanometers wide SWNT pores is expected to be in the Knudsen regime, it was confirmed that 1-cm diameter membranes (three) punched out from the 4-in scale composite displayed N_2 permeance independent of pressure as predicted by Knudsen law.

The obtained permeation data was used to calculate the enhancement factor, defined as the relative ratio of the measured CNT membrane permeance over the Knudsen diffusion prediction. The Knudsen permeance P_k is given by Equation (3).

$$P_k = \frac{\varepsilon d}{3 \tau L} \left(\frac{8}{\pi M R T} \right)^{1/2} \tag{3}$$

where ε is the porosity, d is the CNT inner diameter, τ is the tortuosity, R is the universal gas constant, T is temperature, L is the membrane thickness, and M is the molar mass of the gas. In these calculations, the authors assumed a tortuosity of 1.25 based on the previous results.[29]

Water Permeance and Selectivity Measurements: Representative membranes mounted on Kapton–HN frames were pressurized at 4 psi with a controlled in-house N_2 line in a dead-end filtration cell. Water permeance was quantified as the increase of the permeate weight in a collection vial over time. The corresponding enhancement factor for water permeation

**ADVANCED
SCIENCE NEWS**

www.advancedsciencenews.com

**ADVANCED
FUNCTIONAL
MATERIALS**

www.afm-journal.de

was defined as the relative ratio of the measured per-CNT flow rate (membrane flow rate normalized by the CNT number density) over the estimated transport rate assuming no-slip Hagen–Poiseuille flow.

$$Q_{hp} = \frac{\pi \left(\frac{d}{2}\right)^4 \Delta p}{8 \mu L \tau} \tag{4}$$

where d is the average inner CNT diameter, Δp is the pressure drop across the membrane (~0.28 bar), μ is the dynamic viscosity of water at the experimental temperature of 21 °C (9.76×10^{-4} Pa s), L is the membrane thickness (34.8 ± 0.3 μm), and τ is the tortuosity (1.25).

To characterize the selectivity of our membranes, the rejection coefficient for the negatively charged dye Direct Blue 71 (DB71, Sigma Aldrich, product #212407; molecular size: $3 \times 1.5 \times 1$ nm; concentration: 10 μM aqueous solution) and for the neutral 5-nm diameter polyvinylpyrrolidone (PVP)-capped Au nanoparticles (0.06 mg mL^{-1}, Nanopartz Inc.) were measured, as previously reported.[29,30] The size of the latter probe analyte was just above the maximum CNT pore diameter measured by TEM. DB71 and Au nanoparticles aqueous feed solutions were pressurized at 4 psi in the same dead-end filtration cell used for water permeance quantification. After filtration, the permeate was analyzed by UV–vis spectroscopy (Cary 100 UV–vis spectrophotometer, Agilent; scan spacing: 1 nm; scan range: 200–800 nm) to determine the analyte concentration and then the rejection coefficient (R) was calculated using the following equation.

$$R = 1 - \frac{A_P}{A_F} \tag{5}$$

where A_P and A_F are the absorbances of the permeate and feed solution, respectively, at the peak wavelength $\lambda = 587$ nm for DB71 and $\lambda = 522$ nm for Au nanoparticles. Tests performed with representative ≤ 1 cm^2 membrane samples confirmed that the membranes used in this study were defect-free ($R \geq 99.5\%$ for both analytes).

Solute Diffusion Measurements: The diffusion-driven solute transport measurements across the fabricated CNT membrane were performed as previously reported in detail elsewhere.[52,68–72] The setup used for diffusion measurements was a customized 7 mL Side-Bi-Side glass diffusion cell (PermeGear, Inc.) with a 5 mm orifice as shown in Figure S1, Supporting Information. The CNT membrane (≈ 1.6 cm diameter) was installed between two diffusion cells, followed by clamping the diffusion system. Prior to the measurement, the system was washed with pure ethanol (200 proof) three times and then with deionized (DI) water five times. During the measurement, the liquids in both cells were stirred vigorously at 1500 rpm with magnetic Teflon-coated stir bars to minimize concentration polarization. Four model solutes covering a range of sizes were specifically selected for the transport measurement: KCl (salt, hydrated diameter of K$^+$ ≈ 0.662 and Cl$^-$ ≈ 0.664 nm, 74.55 Da),[18] vitamin B12 (B12, vitamin, ≈ 1–1.5 nm, 1355 Da),[18,52] lysozyme (Lz, egg white, ≈ 3.8–4 nm, 14.3 kDa),[52] and bovine serum albumin (BSA, protein, ≈ 4–14 nm, average Stokes diameter ≈ 7 nm, 66 kDa).[53]

For measuring diffusion-driven KCl (Fisher Chemical, 7447-40-7) transport, KCl solution (0.5 mol L^{-1} in DI water) was filled into the left cell (feed side) and DI water was filled into the right cell (permeate side), with a conductivity meter probe (attached to a Mettler Toledo SevenCompact S230 conductivity benchtop meter) immersed in the permeate side to measure the conductivity every 15 s for 15 min.[52,68–71] For measuring diffusion-driven B12 (Sigma-Aldrich, 68-19-9) or Lz (Bio-world, 12650-88-3) transport, the organic molecule solution (1 mmol L^{-1} in 0.5 mol L^{-1} KCl) was filled into the feed side and KCl solution (0.5 mol L^{-1}) was filled into the permeate side.[52,68–71] For measuring diffusion-driven BSA (Fisher Scientific, BP9703-100) transport, BSA solution (1 mmol L^{-1} in 1× PBS) was filled into the feed side and PBS solution (1×) was filled into the permeate side. A fiber optic dip probe (attached to an Agilent Cary 60 UV–vis Spectrophotometer) was immersed in the permeate side to record the absorbance spectra of organic molecules (B12, Lz, or BSA) in the range of 190 to 1100 nm every 15 s for 40 min.[52,68–71] Different UV–vis wavelengths were used for measuring the intensity changes of each species: 710 nm for

DI water (reference wavelength),[52,68–71] 360 nm for B12,[52,68–71] 282 nm for Lz,[52,68–71] and 278 nm for BSA,[73,74] respectively. The flow rate of each solute was computed via the slope of concentration change in the permeate side; while the permeance was calculated using $p = \frac{V \times \frac{dC}{dt}}{\Delta C \times A_{\text{effective}}}$, where V is the volume of solution (7 mL), dC/dt is the slope of concentration change in the permeate side, $A_{\text{effective}}$ is the effective area of CNT membrane subjected to diffusion test (5 mm diameter orifice area multiplied by 5% of CNT membrane porosity), and ΔC is the solute concentration difference across CNT membrane. All the measurements were replicated three times to obtain average values and standard deviations.[52,68–71]

Preparation of Feed Solutions for Filtration Measurements: Phosphate-buffered saline (PBS) was prepared by dissolving five PBS tablets (Fisher Scientific, BP2944-100) in 1 L Milli-Q water, which yielded a buffer with a pH value of ≈ 7.4 at 25 °C.

Ficoll 70 was labeled with fluorescein isothiocyanate (FITC) as described previously.[75] Briefly, Ficoll 70 (Sigma-Aldrich, F2878) was dissolved in dimethyl sulfoxide (DMSO, Fisher Scientific, D128-500) at 50 mg mL^{-1}. After dissolution, 1 mg mL^{-1} sodium bicarbonate (Fisher Scientific S233-500) and 5 mg mL^{-1} FITC (Sigma-Aldrich, F7250) were added. The solution was heated in a boiling water bath for 15 min or until the solutes were completely dissolved. The solution was then poured slowly into 10× volume of ethanol (200 proof) and allowed to precipitate overnight with light protection. The precipitate was pelleted by centrifugation and the ethanol was removed. The pellet was dissolved in 2 mL of Milli-Q water at 37 °C until completely dissolved. Finally, the labeled FITC-Ficoll was eluted on an equilibrated desalting column (Sephadex G-25 PD-10) to remove unbound FITC.

BSA feed solution was prepared by dissolving BSA powder (Fisher Scientific, BP9703-100) in PBS to get 40 g L^{-1} solution since this albumin concentration was close to that of human serum albumin (35–50 g L^{-1}).[76]

Platelet-poor plasma was prepared by centrifuging fresh bovine blood at 4 °C. First, eight tubes of bovine blood (40 mL per tube) were filled into centrifuge tubes (50 mL). Next, the tubes were inserted into a Thermo Scientific Sorvall ST 40R Centrifuge with bucket 75003608, and centrifuged with 1800 relative centrifugal force (RCF) at 4 °C for 15 min. After that, the obtained supernatants were transferred into new centrifuge tubes, and the tubes were centrifuged again with 1800 relative centrifugal force (RCF) at 4 °C for 15 min. Finally, the supernatant (platelet-poor plasma, Figure S8, Supporting Information) was collected carefully and stored at −80 °C.

Filtration Experiments using FITC-Ficoll 70 in PBS Solution: The filtration measurements were carried out using a custom-designed pressure-driven cross-flow filtration system as shown in Figure 2A.[54] For membrane installation, the CNT membrane was backed up by a Si mask ($\approx 50\%$ porosity, providing mechanical support), sandwiched between two polydimethylsiloxane (PDMS) gaskets (ensuring the system is leak-free), followed by mounting in the custom-built chamber. Prior to the filtration measurements, the membrane was rinsed with ethanol (200 proof), followed by deionized water (Milli-Q) thoroughly. After calibrating the system pressure, the feed solution was circulated with a rotary pump (Masterflex L/S Easy-Load II, 77201–62) at a rate of 20 mL min^{-1} to minimize the concentration polarization of the feed solution. Different transmembrane pressures, which were generated by compressed dry air, monitored by a pressure sensor, and regulated by a pressure controller, were applied to the inlet side. To ensure that measurements were conducted under a steady-state condition, the initial 0.9 mL permeate was discarded and the corresponding feed and permeate solutions were collected from the inlet valve and outlet tube thereafter.

To measure the filtration performance of the CNT membrane, FITC-Ficoll 70 (0.1 mg mL^{-1} in PBS) solution was used as a neutral filtration probe in the feed side with constant transmembrane pressures (0.3, 0.4, and 0.5 psi) applied to the inlet side.

To measure the filtration performance of the commercial hemofiltration/hemodialysis membrane, a customized dialyzer (see Figure S2, Supporting Information) was fabricated by assembling some commercial high-flux HF400 filtration fibers[7,77] (Renaflo II, Minntech) extracted from the HF400 cartridge. The parameters of the HF400 cartridge, as specified by the manufacturer, are as follows: fiber wall thickness ≈ 50 μm, fiber

inner diameter ≈200 µm, cartridge fiber length ≈120 mm, total cartridge surface area ≈0.3 m², and the sieving coefficients of urea, creatinine, B12, myoglobin, and albumin ≈1.0, 1.0, 0.974, 0.20, and 0.016, respectively. The total areas of the custom-built HF400 dialyzer fibers (≈2–4 cm²) were computed by $Area = P_{inner} \times L \times n$, where P_{inner} is the inner perimeter of hollow fiber, L is the fiber length, and n is the fiber number. FITC-Ficoll 70 solution with the same concentration (0.1 mg mL⁻¹ in PBS) was used as the testing probe. The Ficoll feed was circulated with a rotary pump (Masterflex L/S Small Cartridges for Multichannel Cartridge Pump, EW-07519-85) at a rate of 1 mL min⁻¹, and transported inside the hollow fibers of HF400 dialyzer, while the permeate passed through the fiber wall to the outside of the fiber (Figure S2, Supporting Information). We decrease the flow rate from several hundred mL min⁻¹ (e.g., ≈500 mL min⁻¹ of blood) typically used for the HF400 cartridge to ≈1 mL min⁻¹ (of Ficoll in PBS) for the custom-built dialyzer with HF 400 fibers to account for differences in the total area of cartridge (≈0.3 m²) versus than the customized dialyzer (≈2–4 cm²) while ensuring similar order of magnitude flow rate per unit area. A simple mathematical calculation of flow rate/unit area provided ≈1667 mL min⁻¹ m⁻² for commercial HF400 cartridge and ≈2500–5000 mL min⁻¹ m⁻² for the customized device built using fibers extracted from HF400 dialyzer for comparison. The feed pressure was calculated by averaging the values of two pressure sensors at the top and bottom of the HF400 dialyzer on the feed side, and the transmembrane pressure was maintained the same (0.3, 0.4, and 0.5 psi, respectively) as used in filtration experiments with CNT membrane.

The concentrations of FITC-Ficoll 70 in the feed and permeate were analyzed by size-exclusion chromatography with an Ultrahydrogel 500 column and guard column (Waters, Milford, MA).[54] PBS (150 mmol NaCl, 50 mmol phosphate, 200 ppm NaN₃, pH 7.0) was employed as the mobile phase with a flow rate of 0.5 mL min⁻¹. FITC-Ficoll 70 was analyzed by a fluorescence detector (model G1321A; Agilent Technologies) at excitation/emission (Ex./Em.) 495/520 nm. The relationship between molecular weight and retention time for each time point individually was obtained by using multi-angle light scattering (DAWN TREOS; Wyatt Technology, Santa Barbara, CA) along with differential refractive index (model G1362A; Agilent Technologies), and calculated using ASTRA software.[54]

The sieving coefficient (SC), defined as the ratio of permeate (C_p) to feed concentration (C_f), was computed via $SC = C_p/C_f$. The measured hydraulic permeability (mL h⁻¹ mmHg⁻¹ m⁻²) was obtained by dividing the transmembrane flow rate (mL h⁻¹, measured by the meniscus level change along a graduated syringe on the outlet side) per applied transmembrane pressure (mmHg) by the entire membrane area (m²); while the calculated hydraulic permeability was calculated by taking into account the porosity of membrane (≈5% for CNT and ≈50% for HF400).[78] Error bars showed standard deviation (SD) over multiple measurements. The Darcy permeability[54] was obtained by multiplying calculated hydraulic permeability by the dynamic viscosity of the fluid (≈10⁻³ Pa s for Ficoll in PBS solution) and membrane thickness (34.8 µm for CNT membrane and 50 µm for HF400 membrane).

Filtration Experiments using BSA Solution (in PBS) and Platelet-Poor Plasma: After the above experiments using FITC-Ficoll 70, the filtration system was rinsed thoroughly with PBS solution before measuring the filtration of albumin across the membrane (HF400 or CNT). The sieving performance of BSA during filtration was measured using a BSA solution (40 g L⁻¹ in PBS). Platelet-poor plasma (which contains a high concentration of BSA protein) was also used as the feed to check both the sieving performance of BSA and the plasma compatibility. The filtration experiments were performed using the same methods mentioned above with a little modification on the transmembrane pressure (0.6 psi, rather than 0.3–0.5 psi). A little higher pressure (0.6 psi) was used to do the filtration of BSA because the relatively high oncotic pressure (≈0.3–0.5 psi)[79,80] from the BSA solution or plasma feed creates a driving force counter to the pressure differential. The feed and permeate solutions were collected from the inlet valve and outlet tube, respectively. For BSA in PBS solution, the permeate was evaluated with Bradford Protein Assay[59] using a standard assay ratio (10 µL of sample to 300 µL of Coomassie dye) by a Nanodrop one Microvolume UV–vis Spectrophotometer (Thermo Scientific). Error bars showed SD over multiple measurements. For platelet-

poor plasma, the plasma feed and permeate were evaluated with the SDS-PAGE method.[60] The obtained gel images with separated proteins were recorded using a UVITEC Cambridge Gel documentation system and analyzed using the ImageJ software. Error bars showed SD over multiple measurements.

Hemofiltration Experiments using FITC-Ficoll 70 in Platelet-Poor Plasma: The hemofiltration experiments were performed using the same methods mentioned above with the same raised transmembrane pressure (0.6 psi). FITC-Ficoll 70 in platelet-poor plasma (0.1 mg mL⁻¹) was used as the feed. No visible plasma fouling was observed in the perfusate loop on the feed side after 24 h and avoided using anti-coagulants to minimize experimental variation. The feed and permeate solutions were collected from the inlet valve and outlet tube, respectively. The concentrations of FITC-Ficoll 70 in the feed and permeate were analyzed by the same size-exclusion chromatography.[54] DI water was used in between the samples to wash the column (remove protein residues). The sieving coefficient and hydraulic permeability were computed using the same methods described above.

Heteroselective Model: Solute sieving as a function of solute size a across a heteroselective membrane could be characterized by a continuous distribution $\Omega(r)$ of size-selective elements with size r as follows.

$$s(a) = \int_0^\infty \theta(a,r)\, \Omega(r)\, dr \tag{6}$$

where $\theta(a,r)$ is a sieving function describing transport processes across a single size-selective element, and the $s(a)$ are usually experimental sieving coefficients for various solute sizes. Equation (6) might be rewritten as an integral operator K acting via Ω resulting in the sieving curve.

$$s = K[\Omega] \tag{7}$$

If K is invertible, one could calculate the size distribution from $\Omega = K^{-1}[s]$. Transfer of a non-ionic spherical solute species across a cylindrical pore with pore radius r had a well-known[81] sieving function for each individual pore.

$$\theta(a,r) = \frac{W(a,r)}{1 - (1 - W(a,r))\, e^{-Pe}} \tag{8}$$

Assuming laminar flow, the Péclet number was given by the following equation.

$$Pe = \frac{W(a,r)}{H(a,r)\, D(a)} \left(\frac{r^2}{8\eta}\right) \Delta P \tag{9}$$

where W and H are hindrance factors[82] for cylindrical pores, ΔP the driving pressure (kPa), and η is the viscosity of the permeate (Pa·s). The variation in hydrodynamic size of the flexible polysucrose molecules was described by a continuous log-normal distribution $G_{R,a,\xi}$, as follows.

$$H(a,r)\, D(a) = \int_0^\infty H_{iso}(R,r)\, D_\infty(R)\, dG_{R,a,\xi} \tag{10}$$

$$W(a,r) = \int_0^\infty W_{iso}(R,r)\, dG_{R,a_i,\xi} \tag{11}$$

Here, integration was in the Riemann–Stieltjes sense and $G_{R,a_i,\xi} = $ erfc(-log(R/a_i)/log(ξ)/$\sqrt{2}$)/2 where R and ξ are the geometric mean and standard deviation of the distribution, respectively; H_{iso} and W_{iso} are isoporous hindrance factors described by Dechadilok and Deen;[82] D_∞ the diffusion coefficient in free solution $D_\infty = kT/(6\pi\eta_w a_i)$ where $T = 293$ K, $\eta_w = 1$ mPa·s, a_i the Stokes–Einstein radius, k is the Boltzmann constant, and r is the unrestricted pore radius.

Solute Sieving in Carbon Nano-Tubes: The extreme convection in CNTs meant that Peclet numbers were sufficiently large so that diffusion could safely be neglected, that is, $\theta_{i,j} \approx W_{i,j}$. Under these conditions, sieving coefficients were described as follows.

$$\theta(a, r) = \int_0^\infty W_{CNT}(R, r)\, dG_{R,a,\xi} \tag{12}$$

where W_{CNT} is the convective restriction function for the CNT membrane. Suitable expressions for W_{CNT} were as yet unknown, but on the basis of experimental data, it was found that the following type of functions described solute sieving in CNT membranes remarkably well.

$$\theta(a, r) = \frac{1}{2}\mathrm{erfc}\left(\frac{\log\frac{a}{r+q}}{\sqrt{2}\log\xi}\right) \tag{13}$$

This function took into account the flexibility of the molecules (ξ)[61] but also the deformability defined by $q \in \mathbb{R}^+$ corresponding to the displacement (right shift in nm) from the expected sieving curve. It was thus assumed that, under the high flow rates in CNTs, polysucrose molecules were deformed allowing them to permeate much smaller pores than that of their Stokes radius. However, in their deformed state, they retained the molecular flexibility of their non-deformed state.

Supporting Information

Supporting Information is available from the Wiley Online Library or from the author.

Acknowledgements

Conflict of Interest

The authors declare no conflict of interest.

Author Contributions

P.R.K. set up the collaborative project with input on methods from W.H.F and N.F. and CNT membranes from LLNL. P.C. and N.F. performed the filtration (Ficoll and BSA in PBS)/hemofiltration (bovine blood plasma and Ficoll in plasma) experiments and all associated characterizations. P.C. performed diffusion-driven transport experiments with different solutes. N.F. and D.W. synthesized FITC-Ficoll 70. S.R. fabricated the Si masks. S.J.P. synthesized the CNT forests and performed structural characterization (TEM, SEM, and Raman). S.F.B., M.L.J., and F.F. prepared the CNT membranes and performed transport characterizations (N_2 gas, water/liquid, DB71 dye, and Au nanoparticle rejection). F.F. wrote the parts of the manuscript corresponding to work performed at LLNL. C.M.O. performed the mathematical modeling and wrote the corresponding parts of the manuscript. All authors contributed to data interpretation and discussions. P.C. and P.R.K. wrote and edited the manuscript with input from all authors.

Data Availability Statement

The data that support the findings of this study are available in the supplementary material of this article.

[1] B. Bikbov, C. A. Purcell, A. S. Levey, M. Smith, A. Abdoli, M. Abebe, O. M. Adebayo, M. Afarideh, S. K. Agarwal, M. Agudelo-Botero, E. Ahmadian, Z. Al-Aly, V. Alipour, A. Almasi-Hashiani, R. M. Al-Raddadi, N. Alvis-Guzman, S. Amini, T. Andrei, C. L. Andrei, Z. Andualem, M. Anjomshoa, J. Arabloo, A. F. Ashagre, D. Asmelash, Z. Ataro, M. M. W. Atout, M. A. Ayanore, A. Badawi, A. Bakhtiari, S. H. Ballew, et al., *Lancet* **2020**, *395*, 709.

[2] E. F. Carney, *Nat. Rev. Nephrol.* **2020**, *16*, 251.

[3] R. L. Mehta, J. Cerdá, E. A. Burdmann, M. Tonelli, G. García-García, V. Jha, P. Susantitaphong, M. Rocco, R. Vanholder, M. S. Sever, D. Cruz, B. Jaber, N. H. Lameire, R. Lombardi, A. Lewington, J. Feehally, F. Finkelstein, N. Levin, N. Pannu, B. Thomas, E. Aronoff-Spencer, G. Remuzzi, *Lancet* **2015**, *385*, 2616.

[4] C. Ronco, W. R. Clark, *Nat. Rev. Nephrol.* **2018**, *14*, 394.

[5] N. A. Hoenich, C. Woffindin, J. N. S. Matthews, M. E. Goldfinch, J. Turnbull, *Nephrol., Dial., Transplant.* **1994**, *9*, 60.

[6] N. A. Hoenich, C. Woffindin, S. Stamp, S. J. Roberts, J. Turnbull, *Biomaterials* **1997**, *18*, 1299.

[7] Z. Liao, E. Klein, C. K. Poh, Z. Huang, J. Lu, P. A. Hardy, D. Gao, *J. Membr. Sci.* **2005**, *256*, 176.

[8] F. Maduell, L. Rodas, J. J. Broseta, M. Gomez, M. Xipell, E. Guillen, E. Montagud-Marrahi, M. Arias-Guillén, N. Fontseré, M. Vera, N. Rico, *Blood Purif.* **2019**, *48*, 167.

[9] R. L. Mehta, B. Mcdonald, F. B. Gabbai, M. Pahl, M. T. A. Pascual, A. Farkas, R. M. Kaplan, *Kidney Int.* **2001**, *60*, 1154.

[10] M. Belmouaz, M. Bauwens, T. Hauet, V. Bossard, P. Jamet, F. Joly, E. Chikki, S. Joffrion, E. Gand, F. Bridoux, *Nephrol., Dial., Transplant.* **2020**, *35*, 328.

[11] A. Boschetti-de-Fierro, M. Voigt, M. Storr, B. Krause, *Sci. Rep.* **2015**, *5*, 18448.

[12] A. H. Kirsch, R. Lyko, L.-G. Nilsson, W. Beck, M. Amdahl, P. Lechner, A. Schneider, C. Wanner, A. R. Rosenkranz, D. H. Krieter, *Nephrol., Dial., Transplant.* **2017**, *32*, 165.

[13] A. Boschetti-de-Fierro, M. Voigt, M. Storr, B. Krause, *Int. J. Artif. Organs* **2013**, *36*, 455.

[14] M. Abe, T. Hamano, A. Wada, S. Nakai, I. Masakane, *PLoS One* **2017**, *12*, 0184424.

[15] X. Yu, L. Shen, Y. Zhu, X. Li, Y. Yang, X. Wang, M. Zhu, B. S. Hsiao, *J. Membr. Sci.* **2017**, *523*, 173.

**ADVANCED
SCIENCE NEWS**

www.advancedsciencenews.com

**ADVANCED
FUNCTIONAL
MATERIALS**

www.afm-journal.de

[16] C. Shi, Y. Zhu, Y. Su, L. W. K. Chung, T. Cheng, *Drug Discovery Today* **2009**, *14*, 25.

[17] T. B. Drüeke, *Nephrol., Dial., Transplant.* **2000**, *15*, 17.

[18] L. Wang, M. S. H. Boutilier, P. R. Kidambi, D. Jang, N. G. Hadjiconstantinou, R. Karnik, *Nat. Nanotechnol.* **2017**, *12*, 509.

[19] L. Prozorovska, P. R. Kidambi, *Adv. Mater.* **2018**, *30*, 1801179.

[20] P. R. Kidambi, P. Chaturvedi, N. K. Moehring, *Science* **2022**, *374*, abd7687.

[21] M. Wolley, M. Jardine, C. A. Hutchison, *Clin. J. Am. Soc. Nephrol.* **2018**, *13*, 805.

[22] M. J. Wolley, C. A. Hutchison, *Nephrol., Dial., Transplant.* **2018**, *33*, iii6.

[23] W. H. Fissell, S. Roy, A. Davenport, *Kidney Int.* **2013**, *84*, 256.

[24] A. C. Castro, M. Neri, A. Nayak Karopadi, A. Lorenzin, N. Marchionna, C. Ronco, *Clin. Kidney J.* **2019**, *12*, 300.

[25] N. To, I. Sanada, H. Ito, G. S. Prihandana, S. Morita, Y. Kanno, N. Miki, *Front. Bioeng. Biotechnol.* **2015**, *3*, 70.

[26] J. Himmelfarb, R. Vanholder, R. Mehrotra, M. Tonelli, *Nat. Rev. Nephrol.* **2020**, *16*, 573.

[27] J. Himmelfarb, B. Ratner, *Nat. Rev. Nephrol.* **2020**, *16*, 558.

[28] J. K. Holt, H. G. Park, Y. Wang, M. Stadermann, A. B. Artyukhin, C. P. Grigoropoulos, A. Noy, O. Bakajin, *Science* **2006**, *312*, 1034.

[29] N. Bui, E. R. Meshot, S. Kim, J. Peña, P. W. Gibson, K. J. Wu, F. Fornasiero, *Adv. Mater.* **2016**, *28*, 5871.

[30] M. L. Jue, S. F. Buchsbaum, C. Chen, S. J. Park, E. R. Meshot, K. J. J. Wu, F. Fornasiero, *Adv. Sci.* **2020**, *7*, 2001670.

[31] Y. Li, C. Chen, E. R. Meshot, S. F. Buchsbaum, M. Herbert, R. Zhu, O. Kulikov, B. McDonald, N. T. N. Bui, M. L. Jue, S. J. Park, C. A. Valdez, S. Hok, Q. He, C. J. Doona, K. J. Wu, T. M. Swager, F. Fornasiero, *Adv. Funct. Mater.* **2020**, *30*, 2000258.

[32] S. F. Buchsbaum, M. L. Jue, A. M. Sawvel, C. Chen, E. R. Meshot, S. J. Park, M. Wood, K. J. Wu, C. L. Bilodeau, F. Aydin, T. A. Pham, E. Y. Lau, F. Fornasiero, *Adv. Sci.* **2021**, *8*, 2001802.

[33] F. Fornasiero, H. G. Park, J. K. Holt, M. Stadermann, C. P. Grigoropoulos, A. Noy, O. Bakajin, *Proc. Natl. Acad. Sci. U. S. A.* **2008**, *105*, 17250.

[34] B. Lee, Y. Baek, M. Lee, D. H. Jeong, H. H. Lee, J. Yoon, Y. H. Kim, *Nat. Commun.* **2015**, *6*, 7109.

[35] K. H. Chan, E. T. Wong, M. I. Khan, A. Idris, N. M. Yusof, *J. Ind. Eng. Chem.* **2014**, *20*, 3744.

[36] M. A. Ashraf, A. Islam, M. A. Butt, T. Hussain, R. U. Khan, S. Bashir, J. Iqbal, *Int. J. Biol. Macromol.* **2021**, *191*, 872.

[37] M. Ioniță, L. E. Cristǎ, S. I. Voicu, S. Dinescu, F. Miculescu, M. Costache, H. Iovu, *Carbohydr. Polym.* **2018**, *183*, 50.

[38] M. Irfan, A. Idris, N. M. Yusof, N. F. M. Khairuddin, H. Akhmal, *J. Membr. Sci.* **2014**, *467*, 73.

[39] C. Nie, L. Ma, Y. Xia, C. He, J. Deng, L. Wang, C. Cheng, S. Sun, C. Zhao, *J. Membr. Sci.* **2015**, *475*, 455.

[40] X. Yu, Y. Zhu, C. Cheng, T. Zhang, X. Wang, B. S. Hsiao, *J. Membr. Sci.* **2019**, *582*, 151.

[41] M. N. Z. Abidin, P. S. Goh, A. F. Ismail, M. H. D. Othman, H. Hasbullah, N. Said, S. H. S. A. Kadir, F. Kamal, M. S. Abdullah, B. C. Ng, *Mater. Sci. Eng., C* **2016**, *68*, 540.

[42] M. Irfan, M. Irfan, S. M. Shah, N. Baig, T. A. Saleh, M. Ahmed, G. Naz, N. Akhtar, N. Muhammad, A. Idris, *Mater. Sci. Eng., C* **2019**, *103*, 109769.

[43] S.-C. Yen, Z.-W. Liu, R.-S. Juang, S. Sahoo, C.-H. Huang, P. Chen, Y.-S. Hsiao, J.-T. Fang, *ACS Appl. Mater. Interfaces* **2019**, *11*, 43843.

[44] M. Irfan, M. Irfan, A. Idris, N. Baig, T. A. Saleh, R. Nasiri, Y. Iqbal, N. Muhammad, F. Rehman, H. Khalid, *J. Biomed. Mater. Res., Part A* **2019**, *107*, 513.

[45] S. J. Park, K. Moyer-Vanderburgh, S. F. Buchsbaum, E. R. Meshot, M. L. Jue, K. J. Wu, F. Fornasiero, *Carbon* **2023**, *201*, 745.

[46] E. R. Meshot, S. J. Park, S. F. Buchsbaum, M. L. Jue, T. R. Kuykendall, E. Schaible, L. B. Bayu Aji, S. O. Kucheyev, K. J. J. Wu, F. Fornasiero, *Carbon* **2020**, *159*, 236.

[47] H. Matsumoto, S. Tsuruoka, Y. Hayashi, K. Abe, K. Hata, S. Zhang, Y. Saito, M. Aiba, T. Tokunaga, T. Iijima, T. Hayashi, H. Inoue, G. A. J. Amaratunga, *Carbon* **2017**, *120*, 358.

[48] L. Zhang, B. Zhao, X. Wang, Y. Liang, H. Qiu, G. Zheng, J. Yang, *Carbon* **2014**, *66*, 11.

[49] A. Kohls, M. Maurer Ditty, F. Dehghandehnavi, S.-Y. Zheng, *ACS Appl. Mater. Interfaces* **2022**, *14*, 6287.

[50] Comparison of Parylene C, N, and F : Similarities, Differences and Their Application Areas, https://blog.paryleneconformalcoating.com/comparison-of-parylene-c-n-and-f-similarities-differences-and-their-application-areas/ (accessed: July 2023).

[51] M. S. Dresselhaus, G. Dresselhaus, R. Saito, A. Jorio, *Phys. Rep.* **2005**, *409*, 47.

[52] P. R. Kidambi, D. Jang, J.-C. Idrobo, M. S. H. Boutilier, L. Wang, J. Kong, R. Karnik, *Adv. Mater.* **2017**, *29*, 1700277.

[53] S. Ikeda, K. Nishinari, *Biomacromolecules* **2000**, *1*, 757.

[54] N. Ferrell, K. O. Cameron, J. J. Groszek, C. L. Hofmann, L. Li, R. A. Smith, A. Bian, A. Shintani, A. L. Zydney, W. H. Fissell, *Biophys. J.* **2013**, *104*, 1476.

[55] B. Haraldsson, J. Nyström, W. M. Deen, *Physiol. Rev.* **2008**, *88*, 451.

[56] D. Venturoli, B. Rippe, *Am. J. Physiol.* **2005**, *288*, F605.

[57] E. Secchi, S. Marbach, A. Niguès, D. Stein, A. Siria, L. Bocquet, *Nature* **2016**, *537*, 210.

[58] W. H. Fissell, S. Manley, A. Dubnisheva, J. Glass, J. Magistrelli, A. N. Eldridge, A. J. Fleischman, A. L. Zydney, S. Roy, *Am. J. Physiol.* **2007**, *293*, F1209.

[59] M. M. Bradford, *Anal. Biochem.* **1976**, *72*, 248.

[60] U. K. Laemmli, *Nature* **1970**, *227*, 680.

[61] C. M. Öberg, J. J. Groszek, S. Roy, W. H. Fissell, B. Rippe, *Am. J. Physiol.* **2018**, *314*, F1108.

[62] C. M. Öberg, B. Rippe, *Am. J. Physiol.* **2014**, *306*, F844.

[63] L. Lubbad, C. M. Öberg, S. Dhanasekaran, A. Nemmar, F. Hammad, J. Y. Pathan, B. Rippe, O. Bakoush, *Physiol. Rep.* **2015**, *3*, 12397.

[64] C. Rippe, D. Asgeirsson, D. Venturoli, A. Rippe, B. Rippe, *Kidney Int.* **2006**, *69*, 1326.

[65] J. Axelsson, C. M. Öberg, A. Rippe, B. Krause, B. Rippe, *J. Membr. Sci.* **2012**, *413*, 29.

[66] H. Qu, A. Rayabharam, X. Wu, P. Wang, Y. Li, J. Fagan, N. R. Aluru, Y. Wang, *Nat. Commun.* **2021**, *12*, 310.

[67] S. Esconjauregui, R. Xie, M. Fouquet, R. Cartwright, D. Hardeman, J. Yang, J. Robertson, *J. Appl. Phys.* **2013**, *113*, 144309.

[68] P. R. Kidambi, G. D. Nguyen, S. Zhang, Q. Chen, J. Kong, J. Warner, A.-P. Li, R. Karnik, *Adv. Mater.* **2018**, *30*, 1804977.

[69] P. Cheng, M. M. Kelly, N. K. Moehring, W. Ko, A.-P. Li, J. C. Idrobo, M. S. H. Boutilier, P. R. Kidambi, *Nano Lett.* **2020**, *20*, 5951.

[70] P. Cheng, J. Espano, A. Harkaway, A. E. Naclerio, N. K. Moehring, P. Braeuninger-Weimer, P. R. Kidambi, *ACS Appl. Mater. Interfaces* **2022**, *14*, 41328.

[71] P. Cheng, N. K. Moehring, J. C. Idrobo, I. N. Ivanov, P. R. Kidambi, *Nanoscale* **2021**, *13*, 2825.

[72] P. Cheng, F. Fornasiero, M. L. Jue, W. Ko, A.-P. Li, J. C. Idrobo, M. S. H. Boutilier, P. R. Kidambi, *Nat. Commun.* **2022**, *13*, 6709.

[73] V. D. Suryawanshi, L. S. Walekar, A. H. Gore, P. V Anbhule, G. B. Kolekar, *J. Pharm. Anal.* **2016**, *6*, 56.

[74] J. Pang, X. Sha, Y. Chao, G. Chen, C. Han, W. Zhu, H. Li, Q. Zhang, *RSC Adv.* **2017**, *7*, 49361.

[75] M. Ohlson, J. Sörensson, B. Haraldsson, *Am. J. Physiol.* **2000**, *279*, F84.

[76] J. Anguizola, R. Matsuda, O. S. Barnaby, K. S. Hoy, C. Wa, E. DeBolt, M. Koke, D. S. Hage, *Clin. Chim. Acta* **2013**, *425*, 64.

[77] S. S. Dukhin, Y. Tabani, R. Lai, O. A. Labib, A. L. Zydney, M. E. Labib, *J. Membr. Sci.* **2014**, *464*, 173.

[78] M. E. Labib, S. S. Dukhin, *US Patent US10369263B2*, **2019**.

[79] B. M. Koeppen, B. A. Stanton, *1 – Physiology of Body Fluids, (in Renal Physiology, fifth edition)*, Mosby, Philadelphia, PA **2013**.

[80] B. M. Brenner, I. F. Ueki, T. M. Daugharty, *Kidney Int.* **1972**, *2*, 51.

[81] W. M. Deen, *AIChE J.* **1987**, *33*, 1409.

[82] P. Dechadilok, W. M. Deen, *Ind. Eng. Chem. Res.* **2006**, *45*, 6953.